



Oligolayered Co@MXene with a Co \cdots SO₃ cation- π bridge for ultra-rapid catalytic oxidation of a novel “forever chemical” OBS

Shangyi Li, Mengbin Gu, Jun Huang^{*}, Yujue Wang, Gang Yu

State Key Joint Laboratory of Environment Simulation and Pollution Control (SKLESP), Beijing Key Laboratory for Emerging Organic Contaminants Control (BKLEOC), Beijing Laboratory for Environmental Frontier Technologies (BLEFT), School of Environment, Tsinghua University, Beijing 10084, China

ARTICLE INFO

Keywords:

Foamless ozonation
OBS
Co@o-MXene
PMS activation
Co \cdots SO₃ cation- π

ABSTRACT

Sodium *p*-perfluorooctane sulfonate (OBS) as a novel alternative to perfluorooctane sulfonate (PFOS), belongs to the family of per- and polyfluoroalkyl substances (PFASs). We demonstrated that Co-based oligolayered MXene (Co@o-MXene) achieved the complete oxidation of OBS during catalytic ozonation with peroxymonosulfate (PMS). The optimized catalyst exhibited 78.5% OBS oxidation in only 2 min, and the oxidation route was thoroughly investigated by Fukui function calculations and QTOF-MS/MS analysis. However, within the fluoroprotein (FP) foam solution, high TOC removal was performed via the newly designed two-stage ozonation process. Systematic studies indicated that OBS can donate electrons through a Co \cdots SO₃ cation- π bridge on the surface of o-MXene/PMS accompanied by the generation of reactive oxygen species (ROS), the strong adsorption energy (*E*_{ads}) value of PMS, enhanced total density of states (TDOS) and uneven electron density in this reaction system. This work extended the potential of newly developed MXene family materials to decompose PFAS.

1. Introduction

As an alternative to perfluorooctane sulfonate (PFOS) listed in the Annex B of the Stockholm Convention on Persistent Organic Pollutants (POPs), sodium *p*-perfluorooctane sulfonate (OBS) has been widely used in fluoroprotein (FP) foam and oil recovery agents [1, 2]. The annual production of OBS was approximately 3500 tons in China [3]. In the area surrounding Daqing Oilfield in China, OBS was detected at high concentrations in water samples and it was the main contributor to the total per- and polyfluoroalkyl substances (PFASs) concentrations according to the results from Orbitrap HR-MS [4]. As an alternative option of PFOS foam after the Environmental Protection Agency (EPA) restriction, protein foam has been widely used attributing to its relatively low toxicity, low cost and biodegradability. The FP foam was prepared by hydrolyzed protein from animal or vegetable source with preservatives and suitable stabilizers added [5]. The concentration of OBS in FP foam could reach up to above 2 g/L and previous study reported that OBS exposure might lead to metabolic disruption, influence microbial abundance and elicit gut barrier dysfunction in mice [6–8]. Although several studies have characterized contamination from this novel “forever chemical”, few efforts have been made to investigate the

degradation and potential mineralization of OBS [9].

Among the numerous PFAS elimination methods, ozone, with a redox potential of +2.07 V can react with electron-rich regions, such as those present in activated aromatic compounds or in the double bonds of organic molecules. Therefore, ozone has attracted an extensive amount of attention due to its capacity to generate reactive oxygen species (ROS) in situ [10–13]. OBS molecule contained the double bond, phenyl-sulfonate moiety and benzene ring, which could be sites susceptible to O₃ attack. During the use of ozonation for treating PFAS treatment, a key scientific problem is that an abundant amount of foam would be generated via bubble aeration due to the surfactant properties of the PFAS compounds, especially for highly concentrated PFAS-containing waters. The foam formation process might lead to phase transfer occurring at the interface between air and water, and more PFAS could accumulate around bubble [14,15]. Based on this, we developed a new strategy in which the ozone stock solution was prepared in an ice-bath environment and diluted to an optimal concentration to stimulate ozonation reaction. This reaction process was followed by the mixing of the OBS and ozone solution with magnetic stirrers to avoid the kind of foam formation that occurs during the use of aeration technology. However, the typical quantity of \bullet OH generated from the natural O₃

^{*} Corresponding author.

E-mail address: huangjun@mail.tsinghua.edu.cn (J. Huang).

<https://doi.org/10.1016/j.apcatb.2022.121364>

Received 21 January 2022; Received in revised form 28 March 2022; Accepted 29 March 2022

Available online 1 April 2022

0926-3373/© 2022 Elsevier B.V. All rights reserved.

self-decomposition in water is only ~15–30% (i.e., consumed per mole of O_3 might generate ~0.15–0.3 mol of $\bullet OH$) according to previous study [16]. Therefore, various ozone-based advanced oxidation processes (AOPs) have been developed to enhance the degradation of emerging contaminants that are resistant to destruction via a conventional ozonation process [17–19]. The introduction of peroxymonosulfate (PMS) can improve ROS generation and bring sulfate radicals ($SO_4\bullet^-$) with a high redox potential (2.5–3.1 V) and longer lifetime into the ozonation system [20–22]. Additionally, new type of catalysts have been designed and applied in the heterogeneous catalytic process, thus trying to fill the gaps in our understanding of interface reaction mechanism in complex ozone-based technologies, especially against the PFAS substitutes as target pollutants in water.

Inspired by these findings, we proposed that metal cluster grown on a recently developed class of 2D layered MXene as ozone/PMS based AOP catalysts [23]. MXene was synthesized from the extraction of the “A” layers of MAX phases (where M stands for a transition metal, A is assigned to a IIIA or IVA element and X represents C and/or N) [24]. Specifically, MXene, as the supporter of catalysts could combine favorable electrical conductivity properties with hydrophilic surface and lend substantial volumetric capacitance to electrode materials [25]. Furthermore, the layered structure of MXene can provide abundant spaces for the immobilization of active sites, which may improve the distribution on the new carriers and achieve possible applications for these catalysts in water or wastewater treatment [26–28]. Oligolayered MXene (o-MXene) could be successfully prepared using an organic solvent such as dimethyl sulfoxide, tetrabutylammonium hydroxide, facilitating to mass storage capacity [29,30]. Then the electrochemical performance including their high current density and outstanding specific capacities could be observed in previous study [31]. These advantages probably played an important role in the interface electron transfer when the o-MXene was applied as the supporter of catalysts in the AOPs.

Although the crucial roles of the interfacial reaction mechanisms of complex oxidation systems based on new materials coupled with ozone or PMS have been established, much less attention focused on the role of organic pollutants themselves in contributing to their oxidation efficiency, especially in terms of the relationship between optimizing bridge-linked electronic structures and electron transfer [32]. Herein, we investigated the relationship between the functional groups of OBS and electron transfer at a the three-phase interface (ozone, water and solid catalysts). As the electron-donating region, when OBS adsorbs to the surface of metal-based materials, it is reasonable to believe that a special bridging cation- π interaction relevant for the recognition of aromatics can be created to enhance electron transfer and achieve the rapid oxidation of pollutants [33]. Cation- π interactions, as important intermolecular binding forces, have been widely studied in the field of structural biology, supramolecular chemistry and so on according to previous studies [34,35]. Meanwhile, charge transfer has been observed in transition metal ion- π interactions from the perspective of the complexation of transition metal ions with phenolic organic pollutants. Therefore, we tried to investigate and construct π -cation interactions induced by the benzenesulfonic acid groups of OBS and the catalysts based on new material structure, such as metals linked with delocalized π orbitals perpendicular to the plane of the aromatic rings of reduced graphene (rGO) [36]. In this research, accompanied by an electronic microzone with a nonuniform distribution of electrons via the PMS complexation with Co modified o-MXene, the oxidation of OBS was enhanced owing to the polarity-enhanced reaction region introduced via the π -cation interactions during PMS and O_3 activation [37,38]. In addition, this work firstly investigated an actual FP solution including OBS and other coexisting protein components via these new reaction processes and demonstrated the rational regulation of interface reaction mechanism by X-ray absorption fine structure (XAFS), DFT calculations, QTOF-MS/MS and in-situ characterization technology.

2. Experimental section

2.1. Chemicals

The chemical reagents in this research were depicted in [Supplementary Material S1](#) in the [supplementary information](#).

2.2. Preparing the catalysts

The MXene phase synthesis was performed with hydrofluoric acid (HF) to selectively etch Al layers from Ti_3AlC_2 powders according to the previous work [23]. Typically, one gram of as-purchased MAX phase Ti_3AlC_2 was immersed in 10 mL of an aqueous solution of hydrofluoric acid and sealed in a polytetrafluoroethylene cup for three days at 313 K to produce $Ti_3C_2T_x$. After this procedure, the carbide surface layer was terminated by OH, O or F atoms. The obtained material was washed and centrifuged at 3500 rpm for 2 min by deionized water for 3–4 times to remove residual impurities until a suspension pH of ~6 was reached, and then the suspension was dried in a vacuum oven at 333 K overnight and the obtained powder was multilayered $Ti_3C_2T_x$ or $Ti_3C_2T_x$ clay (m-MXene). The m-MXene powders were dispersed in TBAOH aqueous solution (25 wt%) and sonicated for another 3 h at room temperature for intercalation and delamination into the 2D $Ti_3C_2T_x$ nanosheets. After that, the oligolayered $Ti_3C_2T_x$ samples (o-MXene) were obtained and purified by centrifugation and washing several times with deionized water.

The Co@m-MXene and Co@o-MXene composites were synthesized by an impregnation-evaporation method. Briefly, 0.5 g m-MXene or @o-MXene with 350 mg of $Co(NO_3)_2 \cdot 6H_2O$ was successively added to 2.5 mL deionized water. The mixture was stirred vigorously at room temperature for 10 min to obtain the uniform dispersion in the thermostat water bath. Then, the temperature was immediately increased to 343 K to evaporate the water for 40 min. The obtained solid products were constantly ground into uniform powder and transferred to muffle furnace at 473 K for 12 h at a heating rate of 2 K/min. The final catalysts were washed by ultrapure water for several times to eliminate the residual impurities after cooling to ambient temperature. Meanwhile, Co_3O_4 was also prepared by calcining $Co(NO_3)_2 \cdot 6H_2O$ at 473 K for 12 h in air without the addition of m-MXene and o-MXene.

2.3. Characterization

The crystal structure of pure and modified m-MXene and o-MXene were determined by X-ray diffraction (XRD, Bruker D8 Discover, Germany) using Cu K α radiation in 2θ range of 0.5–90°. The morphology and internal structures of different catalysts were investigated by high-resolution transmission electron microscopy (HR-TEM, JEM-2100 F) equipped with energy dispersive X-ray (EDX, X-Max80T, Oxford) and scanning electron microscopy (SEM, JEOL, Japan) measurements. The X-ray absorption fine structure spectra (Co K-edge) in transmission mode of Co@m-MXene and Co@o-MXene were measured at BL14W beamline in Shanghai Synchrotron Radiation Facility (SSRF). The storage rings of SSRF was working with electron energy of 3.5 GeV with a stable current of 200 mA and a double channel-cut Si (111) crystal monochromator. The acquired data of X-ray absorption near-edge structure (XANES) and extended X-ray absorption fine structure (EXAFS) information were analyzed and fitted by the ATHENA module implemented in the FEFFIT software packages for Co. LSV measurements were performed in a typical three-electrode system (0.1 M Na_2SO_4 electrolyte solution) with a CHI 700E electrochemical workstation at room temperature by using saturated Ag/AgCl as the reference electrode and platinum wire as the counter electrode. To prepare the working electrode, 5 mg of the samples and 20 μL of a Nafion solution (5 wt%) were ultrasonically dispersed in 480 μL water and ethanol solution for 20 min. The 7 μL slurry was loaded onto the cleaned glassy carbon electrode as the working electrode. DFT calculation method is shown in

Supplementary Material S2 in the supplementary information.

2.4. Oxidation experiments

Batch experiments were generally carried out in 100 mL polypropylene (PP) conical flasks with covers at room temperature under magnetic stirring (300 rpm). Typically, 10 mg of catalysts and 10 mg of PMS was dispersed into 40.5 mL of ultrapure water. Then, 8.5 mL of saturated ozone water (30 ppm) prepared by the ozone generator (Tonglin, Beijing) was added to trigger the reaction. Immediately, the oxidation experiment was initiated by adding the 1 mL of 1 g/L OBS solution. A 1.0 mL sample was withdrawn at different time intervals (0, 2, 5, 10, 20, 30, 40 min) from the above mixture, filtered through a single-use 0.45- μm polyethersulfone (PES) membrane and quenched with 10 μL of a sodium thiosulfate solution (10 ppm) before analysis. All experiments were performed in triplicate, and the average values of OBS concentrations with standard deviations were presented. The concentration of OBS was quantified by high performance liquid chromatography (HPLC, LC-20AT, Shimadzu, Japan) equipped with a UV/Vis detector at 275 nm. The mobile phase included a 0.02 M dihydrogen phosphate buffer solution and methanol at a ratio of 2:8 (v/v) with a constant elution rate of 1 mL min⁻¹. Methods for detecting the intermediate products during reaction and low concentration of OBS were shown in Supplementary Material S3. EPR (electron paramagnetic resonance), toxicity assessment and OBS oxidation experiments in FP solution were shown in Supplementary Material S4.

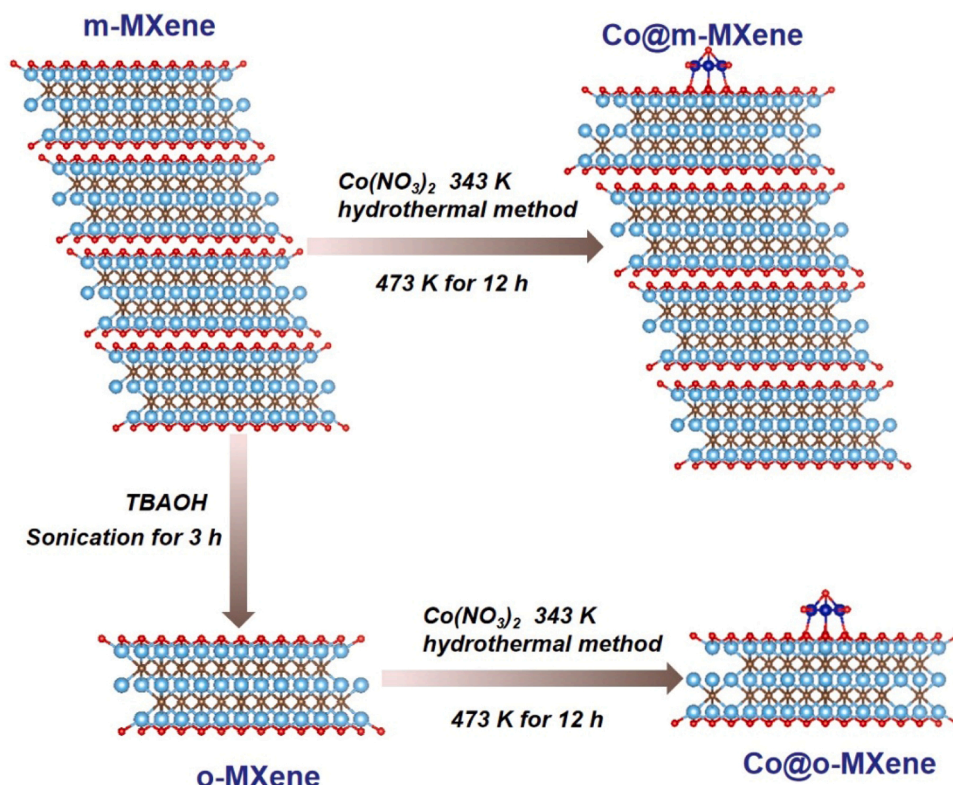
3. Results and discussion

3.1. Characterization

The Co₃O₄ cluster supported on o-MXene was fabricated by a hydrothermal method associated with calcination treatment and this detailed process was shown in Scheme 1. As depicted in Fig. S1 (a), the shift of the MXene characteristic peak in XRD patterns to a lower angle

in accord with the previous study, implying the successful preparation of o-MXene 2D nanosheets [31]. The samples maintained the diffraction peak in comparison with the bare MXene, suggesting the multi-layer MXene and single-layer or oligolayered structure still retained after thermal evaporation and calcination at 473 K. It could be demonstrated that the peaks of Co₃O₄ assigned to the (3 1 1) crystal planes at $2\theta = 36.88^\circ$ with the Co₃O₄ loadings on the surface of m-MXene or o-MXene from Fig. S1 (b) [39]. The morphology of the Co@m-MXene or Co@o-MXene samples was investigated by the SEM images in Fig. 1(a1) and it exhibited that pristine MAX was successfully converted into m-MXene with loose multilayered structure after etching the Al layer by HF acid owing to van der Waals forces. After intercalation with TBAOH and liquid ultrasonication, the bulk Ti₃C₂ would be delaminated into few layered 2D MXene due to ion exchange reaction in Fig. 1(a2). The effectively reduced number of Co@o-MXene layers might provide more exposed active sites for further oxidation reactions. Meanwhile, it could be observed that the loading of Co₃O₄ did not alter the accordion-like structure, which was also evidenced in the TEM patterns (Fig. 1(b1) and (b2)). The detailed analysis of the HRTEM (Fig. 1(c)) image showed that the spacing of the lattice fringes was 0.243 nm, corresponding to the (311) plane of Co₃O₄. The TEM-EDX pattern in Fig. 1(d1)-(d4) exhibited that the main elements of Co@o-MXene structure were Ti, C, O and Co, which were uniformly distributed on carriers in Fig. 1(d5). Furthermore, the nature of Co atoms on the catalysts including chemical state and coordination environment was unveiled by using XAFS measurements.

LSV measurements were carried out to further probe the bulk charge transfer efficiencies of the catalysts in different reaction systems. As indicated in Fig. 2(a) and (b), the current density associated with Co@o-MXene was more apparent than the Co@m-MXene system, ascribed to improved electrical conductivity and rate performance from abundant active sites in the oligolayered Ti₃C₂T_x-T after the delamination of TBAOH. When PMS was injected into the Co@o-MXene or Co@m-MXene system, obviously improved onset current was observed in the catalytic system, implying that electrons would transfer from PMS to Co active sites via the conductive MXene and meanwhile low-dimension



Scheme 1. Illustration of the catalysts preparation.

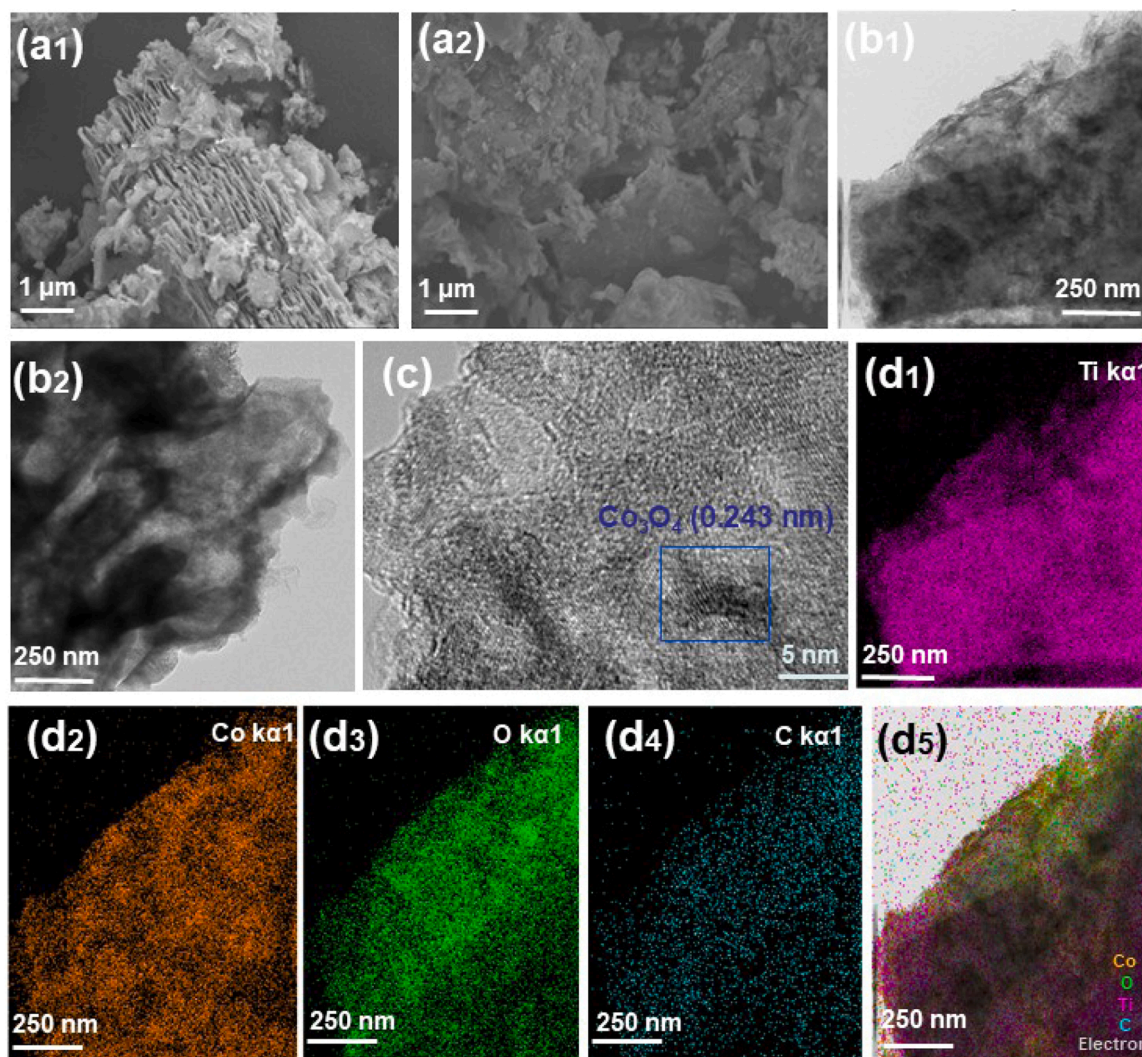


Fig. 1. SEM pattern of Co@m-MXene (a1) and Co@o-MXene (a2). TEM pattern of Co@o-MXene (b1) and Co@m-MXene (b2). HR-TEM of Co@o-MXene (c). Elemental mappings (from TEM) of Co@o-MXene (d1)–(d4). Overlapped elemental mappings Co@o-MXene (d5).

nanosheets provided a better contact with electrons. The charge transfer rate would further increase with the adding of OBS, which manifested the interaction between catalysts and OBS could accelerate the electron transfer to the PMS··Co@o-MXene and thus improved the performance of catalysts during oxidation reaction. Therefore, this result supported the OBS as an electron acceptor in improving the electron transfer efficiency. To verify the interaction between OBS and active sites, Fig. S2 exhibited the FTIR spectroscopy of bare OBS, pure Co@o-MXene and Co@o-MXene/OBS. The sulfonic acid groups brought the characteristic peak of 1160 and 1035 cm^{-1} on the surface of Co@o-MXene/OBS sample in contrast with pure Co@o-MXene. The bands of benzene ring oriented toward adsorbing OBS on Co@o-MXene surface were shifted to lower frequencies (from 1494 to 1450 cm^{-1}), which was the distinct interaction from OBS that complexed with the surface Co via cation- π bonding to the lone pairs of the S-O atoms. The results indicated that OBS complexed with the surface Co via aromatic π bonding on Co@o-MXene and the rich electron would transfer via this special chemical bond on the solid-liquid interface, which agreed well with the results of the in-situ electrochemical experiments.

Fig. 2(c) presented XANES results as the state-of-the-art method to probe the local information of Co K-edge of the Co@m-MXene and Co@o-MXene samples, along with the data for Co and Co_3O_4 as references. It could be observed that the absorption edge of Co@o-MXene (white line) was shifted to the lower energy side by 1.1 eV, which

meant that a decrease of the Co oxidation state might occur when the active Co combined with the delaminated MXene. Furthermore, EXAFS revealed the local environmental evolution of the Co site and the dominant peak represented the Co-O at 1.5–1.7 Å in Fig. 2(d). The coordination number of increased from 3.5 (Co-O) to 4.7 and 4.9 for Co@m-MXene and Co@o-MXene, respectively, in contrast with the standard Co_3O_4 sample according to the results of Table S1. The best-fit analyses illustrated that the Co-Co peaks in the Fourier transform curves of the Co@o-MXene catalyst displayed a decreased peak intensity, implying the altered Co coordination environment in the modified catalysts. Fig. 2(e), (f) and (g) exhibited the wavelet analysis of Co@o-MXene, Co foil and Co_3O_4 , respectively. Co-O and Co-Co coordination were represented by the two main shells of Co atoms and the similar distribution profile of Co@o-MXene and bulk Co_3O_4 could be observed due to a similar coordination structure and similar environment. The distribution profile of Co-Co was largely weakened compared with that of Co@o-MXene, which means that fewer atoms appeared due to the presence of MXene [40,41].

3.2. Catalytic oxidation performance and resistance assessment for application

We believe that the superiority of the OBS oxidation performance of the Co@o-MXene mainly results from the 2D nature of thin structures.

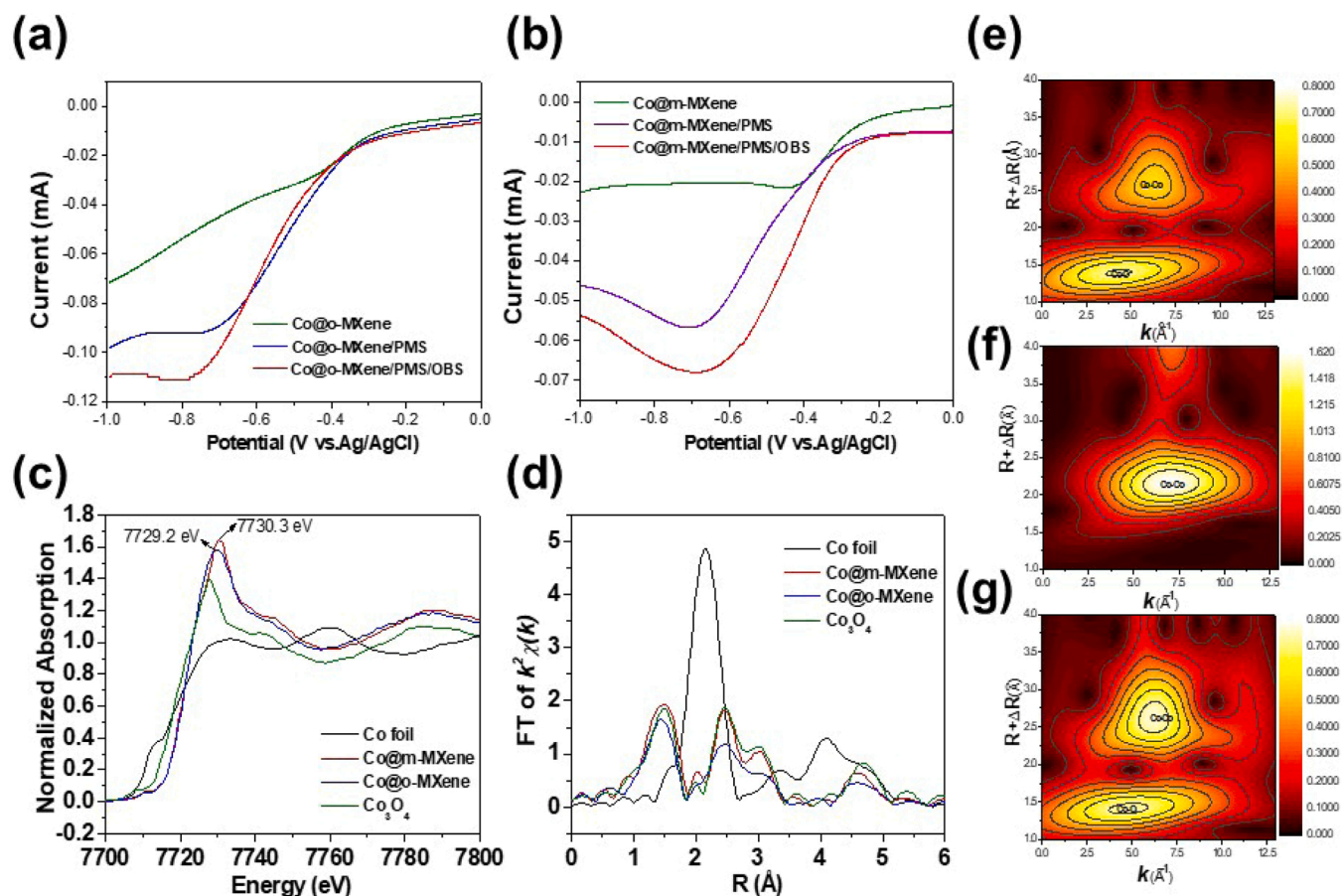


Fig. 2. In-situ LSV of (a) Co@o-MXene and (b) Co@m-MXene in different processes. (c) The Co K-edge XANES spectra of the samples. (d) The curve fitting in R-space from the Co K-edge EXAFS spectra of the samples. Wavelet transform 3D image of Co in (e) Co@o-MXene, (f) Co foil and (g) standard Co₃O₄ samples.

To understand this, Co₃O₄ was loaded on the m-MXene by the thermal evaporation method and the oxidation of OBS in 2 min improved to 57.7%. Notably, the delaminated o-MXene could obviously catalyze the activation of PMS along with O₃ after Co₃O₄ combination and improved the removal of OBS with the percentage oxidation of up to 78.5% in 2 min and even more than 90% OBS oxidation was achieved within 40 min reaction time. Whereas in the system of homogeneous system, the coupling of PMS with O₃ could achieve 39.5% of OBS oxidation at the 40 min reaction time, which was slightly higher than that achieved by ozonation alone (30.22%) owing to the enhanced O₃ chain decomposition by PMS in Fig. 3(a). To differentiate the contribution of oxidation and adsorption, the reaction system was performed under the condition of only catalysts and OBS solution and the removal efficiency of OBS with 300 rpm rotation speed by adsorption was represented. As illustrated in the inserted data in Fig. 3(a), less than 10% OBS was removed by single Co@o-MXene adsorption, which suggested that the adsorption capacity of Co@o-MXene for OBS removal could be neglected. Meanwhile 48.6% of OBS was reduced after the addition of pure Co₃O₄ at the beginning of reaction, which indicated that Co₃O₄ could be as active sites for efficient O₃/PMS activation. The results demonstrated that dimension reduction of MXene played an important role in the application of support-based catalysts during the O₃/PMS based AOPs and the efficiency of Co@o-MXene for the O₃/PMS activation during OBS oxidation was higher than that of Co@m-MXene. To expand scope of catalysts application, we did the degradation experiment of low concentration OBS (ppb level) in the Co@o-MXene/PMS/O₃ process in Fig. S3. The sample was detected by UHPLC/MS-MS and the results showed that nearly 70% OBS could be degraded at only 20 min reaction time when the initial concentration was 6 ppb.

The properties of Co@o-MXene in different content of oxidizing

agent were tested to evaluate the potential application value. In Fig. 3 (b), it can be found that OBS removal increased with the improved amounts of applied ozone in the range of 2.5–10 ppm as prepared by O₃ stock solutions, which was attributed to the enhanced ozone mass transfer that facilitated to ROS generation. However, decreased efficiency of OBS removal might be caused by the presence of excess ozone that might react with •OH when the initial ozone concentration reached to 20 ppm. The reaction efficiency of OBS oxidation increased with the dosage of PMS according to the results of Fig. 3(c). The highest OBS removal (98.1%) at 2 min reaction time was obtained at the PMS dosage of 600 ppm. These enhancements were attributed to the results of a significant amount of ROS generation in the radical pathway associated with PMS activation. Fig. 3(d) showed the effect of Co@o-MXene dosage on the OBS oxidation and degradation efficiency increased from 77.3% to 85.9% as the catalyst concentration increased from 0.05 g/L to 0.1 g/L owing to the greater number of active sites, which was beneficial for adsorption and oxidation degradation. The reaction efficiency was alleviated with the increase of catalyst dosage up to 0.6 g/L at 2 min reaction time. This suggested that higher dosage of catalysts in the Co@o-MXene/PMS/O₃ process was not necessary because that it could not be completely effectively used by PMS/O₃ and the decreased O₃ per unit area was not conducive to the reaction between PMS/O₃ and OBS in solution. Furthermore, excessive catalyst accelerates the consumption of PMS for the generation of SO₅•⁻, leading to lower availability of PMS for the production of SO₄•⁻ [42,43]. Additionally, at higher Co@o-MXene loading, catalyst agglomeration and sedimentation occurred in the solution, which reduced the interfacial area from active sites between reaction solution and samples [44]. Hence, considering the performance of different Co@o-MXene concentration, the catalyst dosage was set to 0.2 g/L in the subsequent experiments.

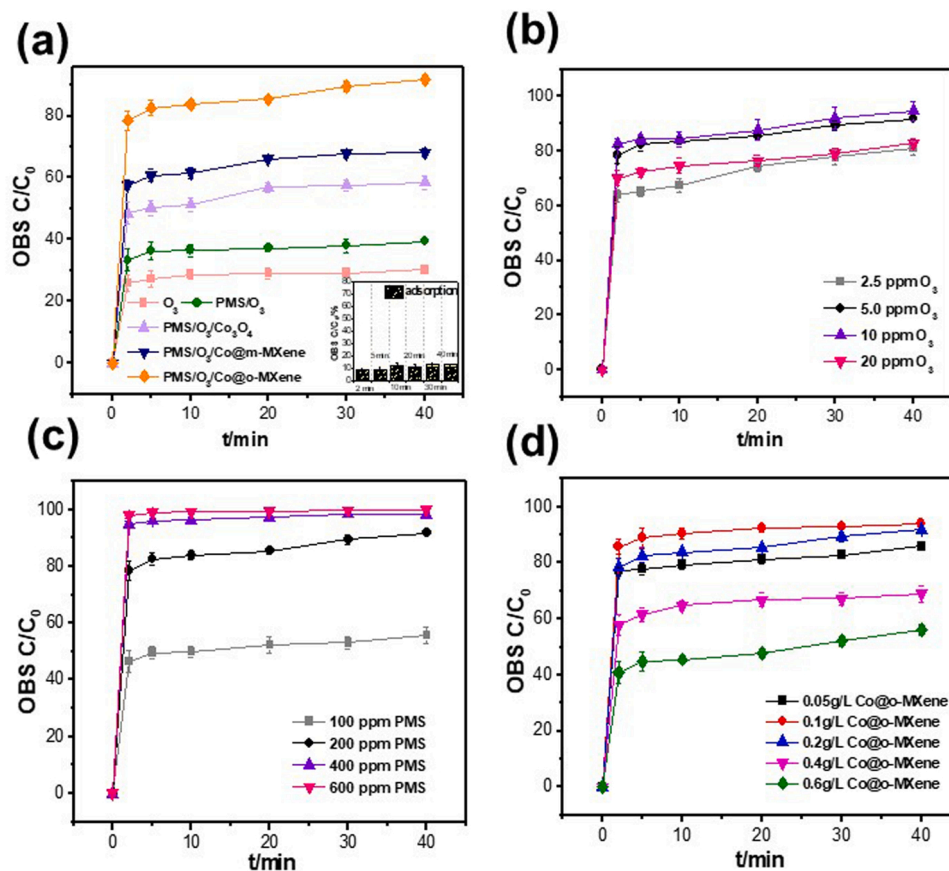
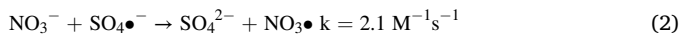
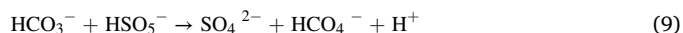
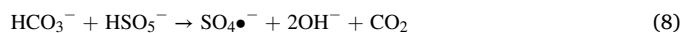
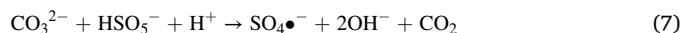
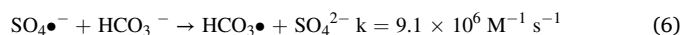
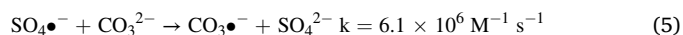
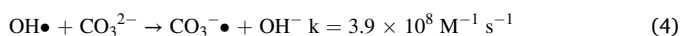
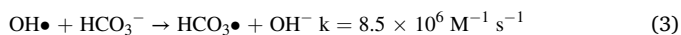


Fig. 3. (a) OBS oxidation by ozonation in different processes (inserted: only Co@o-MXene/OBS process). (b) OBS oxidation in different initial O_3 concentration. (c) OBS oxidation in different initial PMS concentration. (d) OBS oxidation in different initial catalysts concentration. Reaction conditions: [initial OBS] = 20 mg L⁻¹; volume = 100 mL.

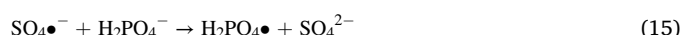
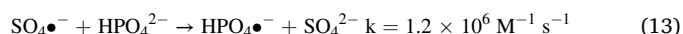
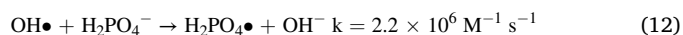
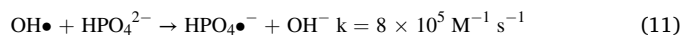
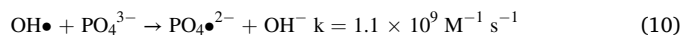
The water matrix played a vital role in the oxidation of target pollutants during heterogeneous catalytic activation of O_3 and PMS processes with different inorganic ions in Fig. 4(a) and (b). It could be observed that the presence of 1, 2 and 4 mM NO_3^- was negligible on OBS oxidation due to the low reaction efficiency between O_3 /PMS and NO_3^- . As shown in Eqs. (1)–(2), the reduction potential of nitrate radicals (2.3 ~ 2.5 V) was slightly lower than OH^\bullet [45]. Compared to some reactive species, such as superoxide radicals, nitrate radicals have higher oxidizing capacity. To sum up, the nitrate ions showed weak influence on the degradation of OBS in the reaction system of Co@o-MXene/ O_3 /PMS.



However, the effect of bicarbonate on the complex oxidation process was investigated and the removal rate of OBS decreased from 91.8% to 42.9% as the bicarbonate content was increased from 1 to 4 mM. These results indicated that the scavenging of $SO_4^{\bullet-}$ and OH^\bullet by HCO_3^- due to the high second-order rate constant (Eqs. (3–9)), which was consistent with the previous studies [46]. The generated $CO_3^{\bullet-}/HCO_3^\bullet$ has weaker redox potential (1.59 V) and higher selectivity compared to OH^\bullet and $SO_4^{\bullet-}$. Thus, inhibition on the degradation of OH^\bullet or $SO_4^{\bullet-}$ induced organic pollutants was usually found. Furthermore, the complexation of metal ions with carbonate ions would restrain the active sites for oxidants, resulting in the decrease of catalytic activity of catalysts [47].



As a strong Lewis base, phosphate may retard the intimate contact of ozone with surface Lewis acid sites of Co@o-MXene, leading to the depression of ozone decomposition according to previous study [48]. Furthermore, phosphate could compete with emerging pollutants by trapping OH^\bullet even though the rate constants of phosphates were not high.



According to Eqs. (10)–(15), OH^\bullet can react with PO_4^{3-} to produce phosphate radicals ($PO_4^{\bullet-}$) and with HPO_4^{2-} to produce hydrogen phosphate radicals ($HPO_4^{\bullet-}$) [49]. Then it combined with dihydrogen phosphate ions would generate dihydrogen phosphate radicals

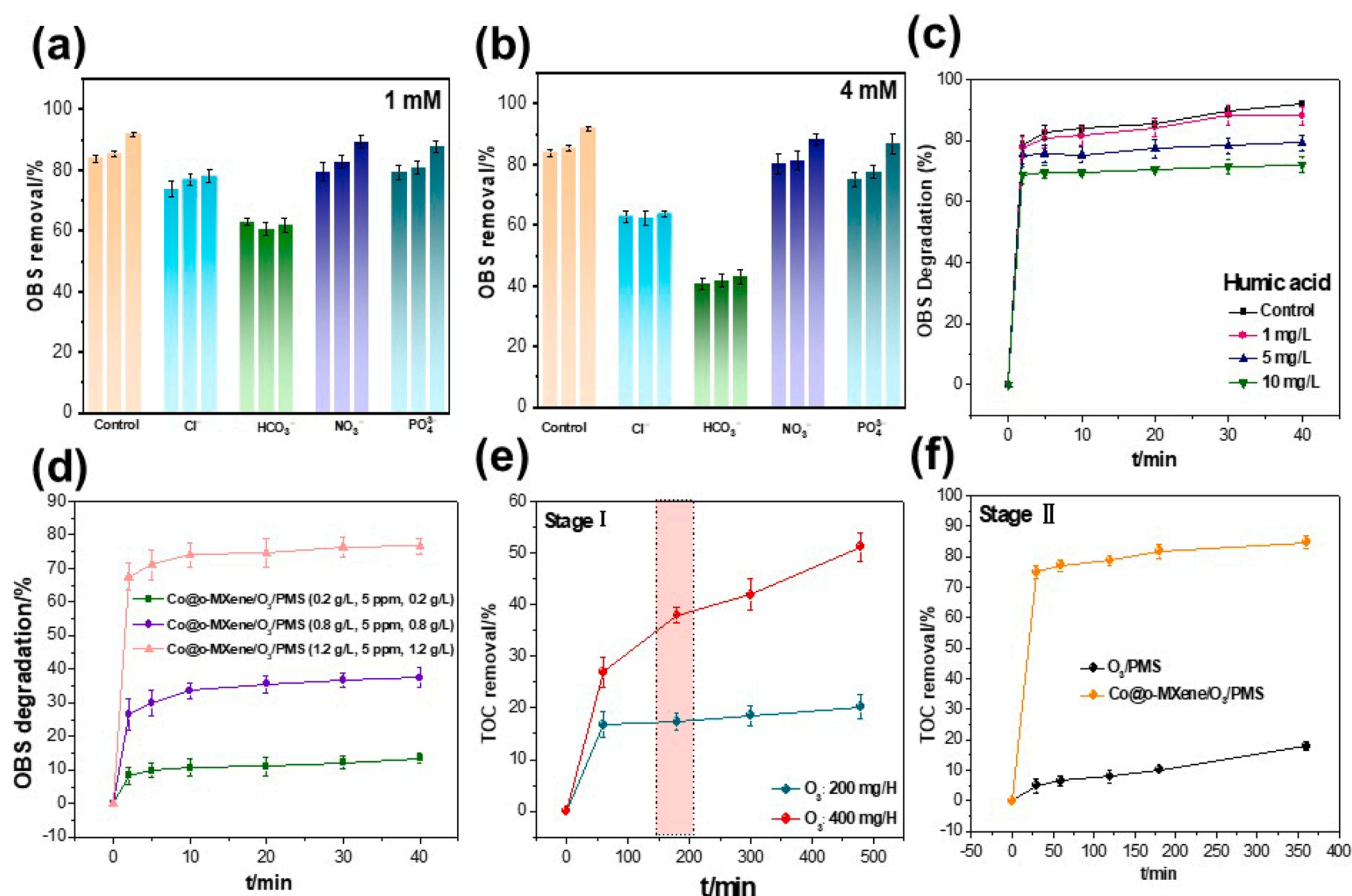
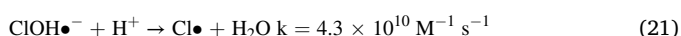
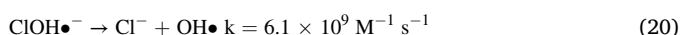
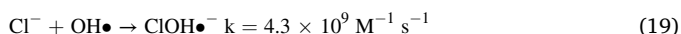
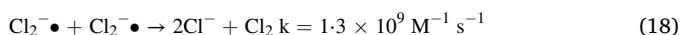
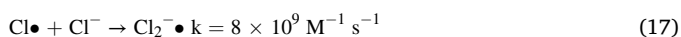
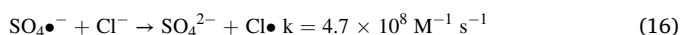


Fig. 4. (a) and (b) The effect of initial different anion concentration, (c) humic acid on OBS oxidation by Co@o-MXene. Reaction conditions: [initial OBS] = 20 mg L⁻¹; Volume = 100 mL; [catalysts] = 0.2 g L⁻¹; [PMS] = 0.2 g L⁻¹; [O₃] = 5 mg/L; initial pH = 3.3. (d) OBS oxidation in FP solution by Co@o-MXene/O₃/PMS. (e) FP solution mineralization in stage I by ozonation alone. (f) FP solution mineralization in stage II by Co@o-MXene/O₃/PMS.

(H₂PO₄•) [50]. Among them, H₂PO₄• has the highest reaction rate with contaminants in water in comparison with HPO₄•⁻ and PO₄•²⁻. However, the presence of phosphate had low inhibitory impact on the OBS removal in heterogeneous catalytic O₃/PMS process and it still showed more than 85% removal with the existence of 4 mM PO₄•³⁻. Similar results could be observed in recent reported study literature that PO₄•³⁻ was probably easy to decompose PMS with lower energy barriers and accelerated the formation of rich SO₄•⁻ for target pollutant oxidation [51]. In addition, a high concentration of Cl⁻ suppressed apparently the removal rate of OBS in this system, which was attributed to that the radical quenching by Cl⁻ to generate chlorine radical with low oxidation capacity and free chlorine species in Eqs. (16–21) [52,53]. Furthermore, it is reported that Cl⁻ would be absorbed on the active sites in the heterogeneous catalytic ozonation system, thus depressing its catalytic activity [21].



Previous study showed that Cl• has lower reduction potential (2.4 V) than hydroxyl radicals (2.8 V). In this case suppression phenomenon on the degradation of some organic pollutants would be observed in the

presence of chloridion. Additionally, it is noted that chloridion has higher selectivity than hydroxyl radicals. In the heterogeneous catalytic system, it could be found that chloridion might form complexation with transient metal ions and affect the adsorption of pollutants on catalysts, which further decreased the performance of AOPs. Meanwhile, the evolutions of oxidation efficiency of OBS in the presence of natural organic matter (NOM) were also provided in Fig. 4(c). Humic acid (HA) was added to the Co@o-MXene/O₃/PMS to assess the impact on the complicated oxidation system. Low concentration of humic acids (1 mg/L) showed the negligible suppression on the oxidation of OBS by the heterogeneous O₃/PMS due to rich ROS generation. The removal rate of OBS in the O₃/PMS process decreased from 88.1% to 71.9% within 40 min when the humic acids concentration was increased from 1 to 10 mg/L. These results indicated that the increase of NOM content could hinder surface-mediated electron transfer on the interface during ozonation in a direct or indirect way, as well as quench the chain reaction owing to the strong scavenging for •OH and SO₄•⁻.

3.3. "Forever chemical" OBS oxidation in an FP solution

The OBS oxidation in realistic FP solution is expected to occur through this Co@o-MXene/PMS/O₃ reaction, involving the TOC removal of FP themselves into nonhazardous H₂O and CO₂. We could observe competitive or scavenging reactions toward the ROS owing to non-PFAS components in the FP foam, including precursors, hydrocarbon surfactants, protein organics and foam stabilizers [54]. As depicted in Fig. 4(d), results presented 76.6% of OBS removal could be achieved when the dosage of both Co@o-MXene and PMS improved from 0.2 g/L to 1.2 g/L at 40 min reaction time. The results implied that the new

heterogeneous reaction system was efficient in the treatment of OBS in a complex reaction matrix containing other organic components when the oxidation reaction conditions were optimized. Considering the high concentration of existing background constituents, even if single OBS could be effectively eliminated, posttreatment technologies would be required to be integrated to this reaction process for TOC removal of FP foam. A two-stage ozonation process was introduced and the ozonation alone (stage I) could consume foaming substances, including OBS or other compounds susceptible to ozone attack. Nearly 40% TOC in solution was removed at 180 min reaction time when the ozone power was increased from 200 to 400 mg/H in Fig. 4(e). Then the FP solution was collected after stage I reaction and it was diluted by a factor of 20 with water for the stage II reaction. At this process, PMS and Co@o-MXene were added to the primed FP solution reaction and the ozone power was decreased to 100 mg/H to stimulate the heterogeneous interface reaction in the PMS/Co@o-MXene/FP system. The presence of catalysts achieved approximately 75% mineralization only within 30 min reaction time, which was much higher than that of the homogeneous ozonation coupling with PMS according to Fig. 4(f).

3.4. Environmental fate properties and reaction route of OBS

Short-chained PFAS showed a shorter persistence time and half-life in water, soil or sediment, which meant that OBS would be more persistent than intermediated products in the environment after release according to EPI Suite software (Table S2). Meanwhile, the acute and

chronic toxicities of OBS and main transformation products during oxidation were also estimated by luminescent bacterial growth inhibition experiments and by using ECOSAR computer program. Fig. S4 showed the toxicity changes of intermediated products for OBS oxidation during O₃/PMS, Co@m-MXene/O₃/PMS and Co@o-MXene/O₃/PMS processes. Around 62.8% and 40.5% of luminescent bacterial growth was inhibited during OBS removal in the O₃/PMS process at 20 and 40 min reaction time, respectively. The presence of Co@m-MXene and Co@o-MXene markedly reduced the toxicity of intermediates owing to the effective oxidation of OBS. Co@o-MXene/O₃/PMS system exhibited only 14.7% of luminescent bacterial growth inhibition at 40 min, which was attributed to the more efficient catalytic reactivity and it was consistent with the Fig. 3(a). Meanwhile, Table S3 presented the calculated ECOSAR class-specific values of acute toxicity (LC50/EC50) and chronic toxicity (ChV) for evaluating the toxicity of the intermediates. The results showed that generated hydroxylated aromatic ring-opening product from catalytic ozonation would lead to their decreased toxicity in comparison with parent OBS. It could be observed that P5 exhibited the highest acute and chronic toxicity for all aquatic organisms among these calculated intermediate products and the corresponded concentration was lowest during Co@o-MXene/O₃/PMS among different processes according to the QTOF-MS/MS results (Fig. S5). These results suggested that the oxidation of OBS using our Co@o-MXene/O₃/PMS process reduced toxicity and produced effluent that was safer for environmental ecosystems than other treatment processes.

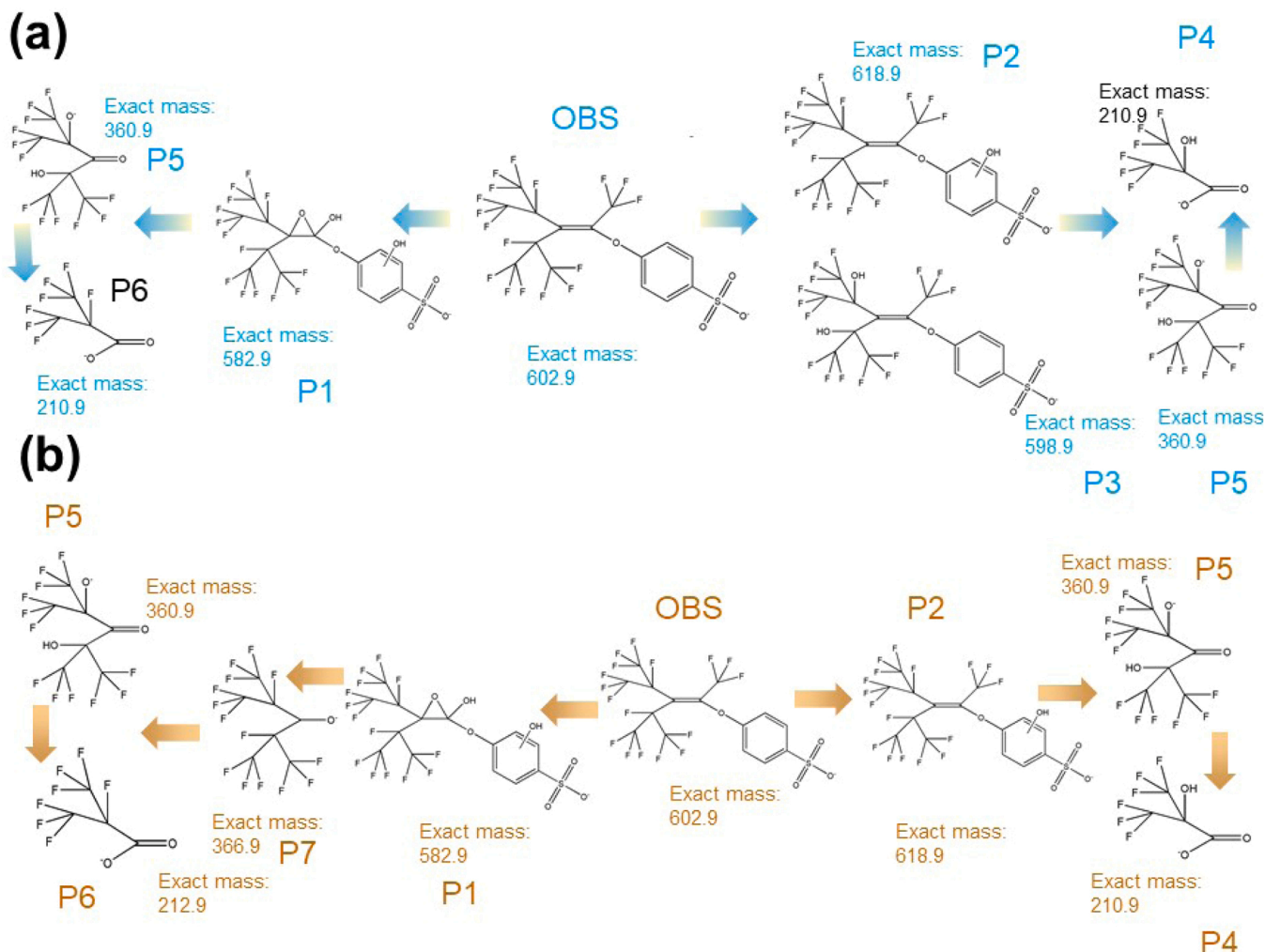


Fig. 5. Reaction pathway of OBS in Co@o-MXene/O₃/PMS (a) and Co@m-MXene/O₃/PMS (b) system.

The possible oxidation pathways in the Co@o-MXene/O₃/PMS and Co@m-MXene/O₃/PMS were proposed by combining with the QTOF-MS/MS results, which were shown in Fig. S6, Fig. 5(a) and (b). We calculated the isosurface of Fukui function of OBS molecule by Gaussian program and the high value of f^-/f^0 obtained indicated a more susceptible potential for electrophilic/ROS attack, which was shown in Fig. 6, Table S4–S10 and Fig. S7–S13. These results indicated that the phenylsulfonate moiety are preferred sites for electrophilic attack (i reaction with $\text{SO}_4^{\bullet-}$ or HO^\bullet) and rich electron cloud could be observed around the benzene ring, C1=C2 and O atom of intermediated products. The calculation of condensed Fukui function f^- demonstrated that the sulfonate moiety is an electron-rich center, and 11 C (0.07745), 18 C (0.07387) and 12 C (0.05605) are the most active sites for ROSS attacking. It could be observed that HO^\bullet addition on benzene ring of OBS to form HO^\bullet adducts (P2, Exact mass, 618.9) in both Co@o-MXene/O₃/PMS and Co@m-MXene/O₃/PMS processes. Meanwhile, the double bond (C1=C2) of OBS was the most likely attacked sites by HO^\bullet radicals and an epoxy group in the intermediate product (P1, Exact mass, 582.9) was formed by elimination of a H_2O molecule after two HO^\bullet addition reaction on C1 and C2 of OBS, which was in consistency with the highest

f^0 value. And P1 are further oxidized to the fluorinated part P7 after double bonds were directly attacked by $\text{SO}_4^{\bullet-}$ or HO^\bullet . However, this part was not detected by QTOF-MS/MS in the processes of Co@o-MXene/O₃/PMS since it would possibly be unstable in water or oxidized quickly by richer oxidizing radical attack in this reaction. Consequently, the P7 product could be further oxidized into ketone at the alcoholic group on C along with simultaneous replacement of F at C3 and C4 by ROSSs to form P5 in Co@m-MXene/O₃/PMS. Meanwhile, this reaction route could be observed by directly attacking under the direct attack of $\text{SO}_4^{\bullet-}/\text{HO}^\bullet$ in Co@o-MXene/O₃/PMS process. During the oxidation of P5, P4 or P6 could be generated by the ketonic group attacking and HO^\bullet replacement on F with further oxidation. The breaking of C–F bonds was hard to occur due to the high energy requirement especially in the oxidation system. However, there are two strong electron-withdrawing CF_3 groups in OBS molecular, which belonged to the branched fluorinated structure and the bond energy of C–F was relatively weak owing to the reduced the electron density. Hence, this would facilitate the electrophilic substitution of F atom by $\bullet\text{OH}$ and $\text{SO}_4^{\bullet-}$, resulting in the rapid decomposition of the molecule to form the product (P3, Exact mass, 598.9) in Co@o-MXene/O₃/PMS.

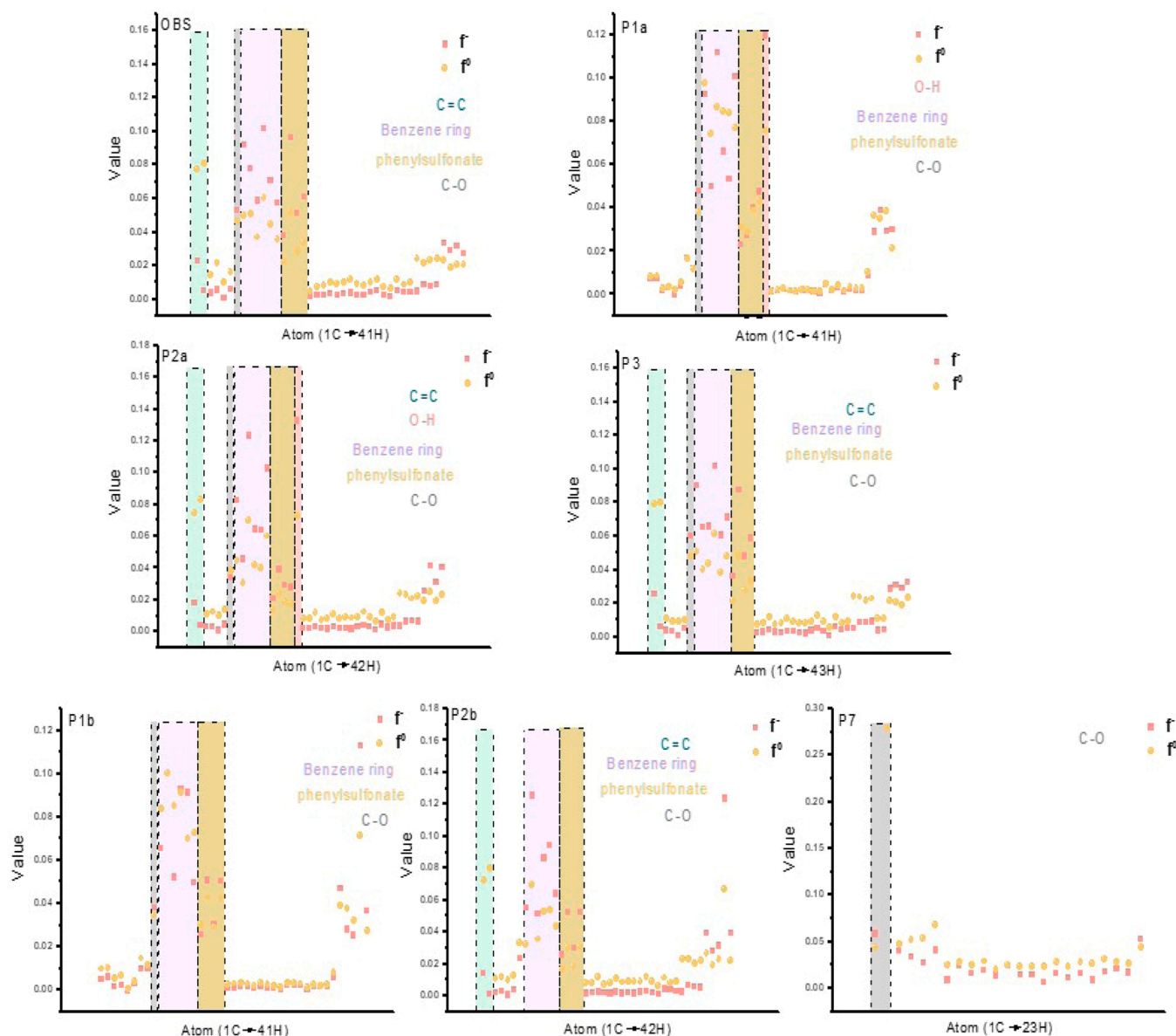


Fig. 6. Fukui function value of OBS and different intermediated products.

3.5. Reaction mechanisms and DFT calculation

Radical quenching experiments were carried out to investigate the role of $^1\text{O}_2$, $\bullet\text{O}_2^-$, $\bullet\text{OH}$ and $\text{SO}_4\bullet^-$ in the oxidation of OBS in the Co@o-MXene/ O_3 /PMS system. Methanol was employed as the scavenger for both $\text{HO}\bullet$ and $\text{SO}_4\bullet^-$. Meanwhile, the presence of TBA could be used to distinguish the contributions from $\bullet\text{OH}$ and $\text{SO}_4\bullet^-$ for the removal of OBS [55]. Fig. S14 showed that the oxidation rate of OBS significantly decreased after adding either 0.4 mM TBA or MeOH, and the oxidation ratio of OBS in Co@m-MXene/ O_3 /PMS decreased to 62.4% and 39.8%, respectively. Higher concentration of 4 mM MeOH or TBA could further inhibit the OBS removal. Therefore, $\bullet\text{OH}$ may be dominant oxidant and contributed more to OBS oxidation than $\text{SO}_4\bullet^-$ in the catalytic ozonation group. It was observed that OBS removal ratio in the Co@o-MXene/ O_3 /PMS systems was still high with the presence of trichloromethane, which may be because that $\bullet\text{O}_2^-$ formed on the surface of catalyst played a minor role in the oxidation of OBS. It exhibited obvious inhibition and only 46.7% OBS was removed with L-Histidine at the 40 min reaction time; thus $^1\text{O}_2$ played an important role in the accelerated oxidation of OBS, indicating that $\bullet\text{OH}$ and $^1\text{O}_2$ were the dominant oxidizing species in the Co@o-MXene/ O_3 /PMS process. Furthermore, the generated ROS by the system of Co@o-MXene/PMS/ O_3 /OBS was verified by the EPR experiment in Fig. S15 [56,57]. And the interface reaction mechanism of ROS was depicted in Scheme 2.

DFT modeling was employed to elucidate the interface reaction occurring at the Co@o-MXene and different reactants, which was shown in Fig. 7(a-f), Fig. S16 and Fig. S17. The possible adsorption configuration and E_{ads} value of PMS, O_3 and OBS on the surface of catalysts were stimulated and the derived E_{ads} was negative in the case of all Co@o-MXene complex compounds, which suggested that the formed structure was stable after the chemisorption process (Table S11). The obtained E_{ads} for PMS on the Co@o-MXene was more negative than that of the other reactants, confirming that a much stronger interaction could be achieved between the active sites and PMS. Thus, the electrostatic attraction between PMS and catalysts could improve the interaction and favor the electron transfer along with enhanced activation efficiency of PMS during oxidation process, which was in accordance with the results of in-situ LSV experiments. The edge and middle O of O_3 molecule were placed on Co@o-MXene clusters with adsorption energies of -1.75 and -0.43 eV, respectively. The results demonstrated the greater potentials of the edge O atom as the excitation site for O_3 decomposition and activation. And the decreased absolute value of calculated E_{ads} suggested that the interaction and charge transfer between the middle O of O_3 and Co@o-MXenes were suppressed. Additionally, a very negative E_{ads} value (-2.21 eV) could be observed after OBS adsorbed to the active

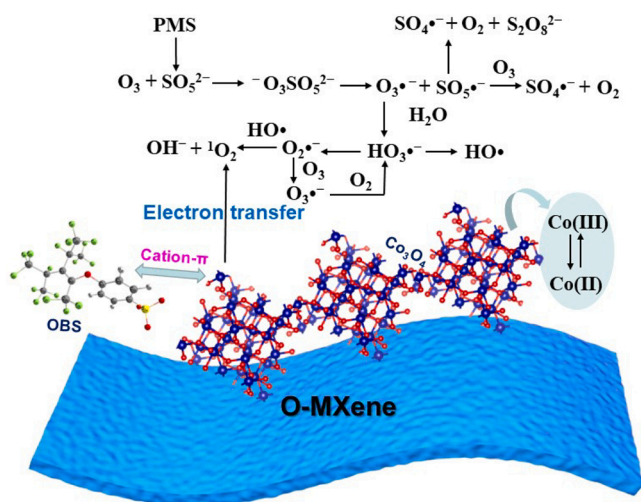
site of catalysts, which implied that the OBS as an electron-donor absorbed on the catalyst could be oxidized through the electron transfer based analogous cation- π (Co-OBS) structure.

In view of the enhanced E_{ads} of O_3 molecule and Co atom in the model of Co@o-MXene clusters, the O_1-O_2 bond length near the metal atom and the O_2-O_3 bond length far away from Co atom were calculated according to the results of Fig. 7(g). Such activated O_3 with longer O_1-O_2 bond on the end O near from Co@o-MXenes than that in the case of the complex of middle O with metal atom or the O_2-O_3 bond, may exhibit stronger oxidizing ability for organic pollutants, thus improving the oxidation performance. Additionally, after PMS adsorption onto Co atom in the models of Co@o-MXene clusters, the $\text{I}_{\text{O}-\text{O}}$ of PMS molecules was increased from 1.41 Å to 1.53 Å, demonstrating that PMS on Co@o-MXene would be more easily to be activated directly than free PMS and this phenomenon indicated that PMS could be cleaved to generate $\text{SO}_4\bullet^-$ and other ROS by multiple oxidizing agents in this heterogeneous catalytic system. The E_{ads} agreed well with the variation of bond length, based on the cation- π (Co-OBS) structure when OBS was adsorbed on the PMS/Co@o-MXene clusters. Additionally, the analysis of bond angle (\angle) before and after the complexation of OBS was investigated. In contrast with the free OBS molecule, the bond angle $\angle\text{C}-\text{O}-\text{C}$ increased from 116.62° to 121.36° in the bond bridge formed by PMS coupled with the Co atom, which was indicative of a strong twisting or bending of OBS and it was desirable for the bond cleavage of OBS via the oxidation reaction.

The differential charge densities of Co@o-MXene/PMS and Co@o-MXene/OBS/PMS intuitively confirmed that abundant electrons gathered at the Co- SO_3 cation- π bridge after OBS complexation, which was shown in Fig. 7(h), (i) and S18. A distinct redistribution of electrons occurred on the unique interface, the electrons would transfer from PMS to the nearby Co-O cluster and the increased charge depletion around the O in Co-O cluster illustrated that the electrons would be captured near Co and even the O atom in SO_3 via the cation- π bridge for the Co@o-MXene/OBS/PMS. Thus, this uneven electron density distribution could effectively regulate the interfacial charge transfer behaviors, increase the surface electron density, and benefit the catalytic oxidation. Fig. S19-S21 exhibited the band charge density distribution in the different composites to identify the relationship in electron transfer via Co- SO_3 cation- π bridge and PMS. The highest occupied energy band (HOEB) and the lowest unoccupied energy band (LUEB) were occupied by Co-O clusters in Co@o-MXene/PMS and Co@o-MXene/OBS clusters. However, HOEB in Co@o-MXene/OBS/PMS was occupied by the Co- SO_3 cation- π bridge, OBS molecular orbital, which could be easily excited to the LUEB as the Co@o-MXene was exposed to PMS and OBS solution. Furthermore, the total density of states (TDOS) of C atoms in Co@o-MXene/PMS and Co@o-MXene/PMS/OBS were presented in Fig. 7(j) and (k). It could be obviously observed that the density of states enhanced significantly in the energy range of $4.3-2.0$ eV in the presence of OBS, suggesting an elevated catalytic activity as a result of interaction of Co- SO_3 cation- π [58]. Furthermore, after OBS complex, the spin down TDOS near the Fermi level in Co@o-MXene/PMS/OBS was higher than that in Co@o-MXene/PMS system, especially for the O p density of states, which was expected to further improve the catalytic reactivity in the bridged bonding area.

4. Conclusion

As a little studied PFAS, OBS poses a potential exposure risk to the local environment owing to similar persistence or bioaccumulation potential with legacy PFOS molecules. Therefore, a novel interface foamless ozonation with PMS activation was developed, which exhibited excellent catalytic performance for OBS oxidation when combining with the Co@o-MXene. Meanwhile, we carried out the OBS removal (76.6%) in FP solution and TOC removal of FP (75%) via this Co@o-MXene/PMS/ O_3 reaction process. QTOF-MS/MS along with the Fukui function calculation results showed that the C=C bond and the benzene ring



Scheme 2. Illustration of catalytic reaction mechanism.

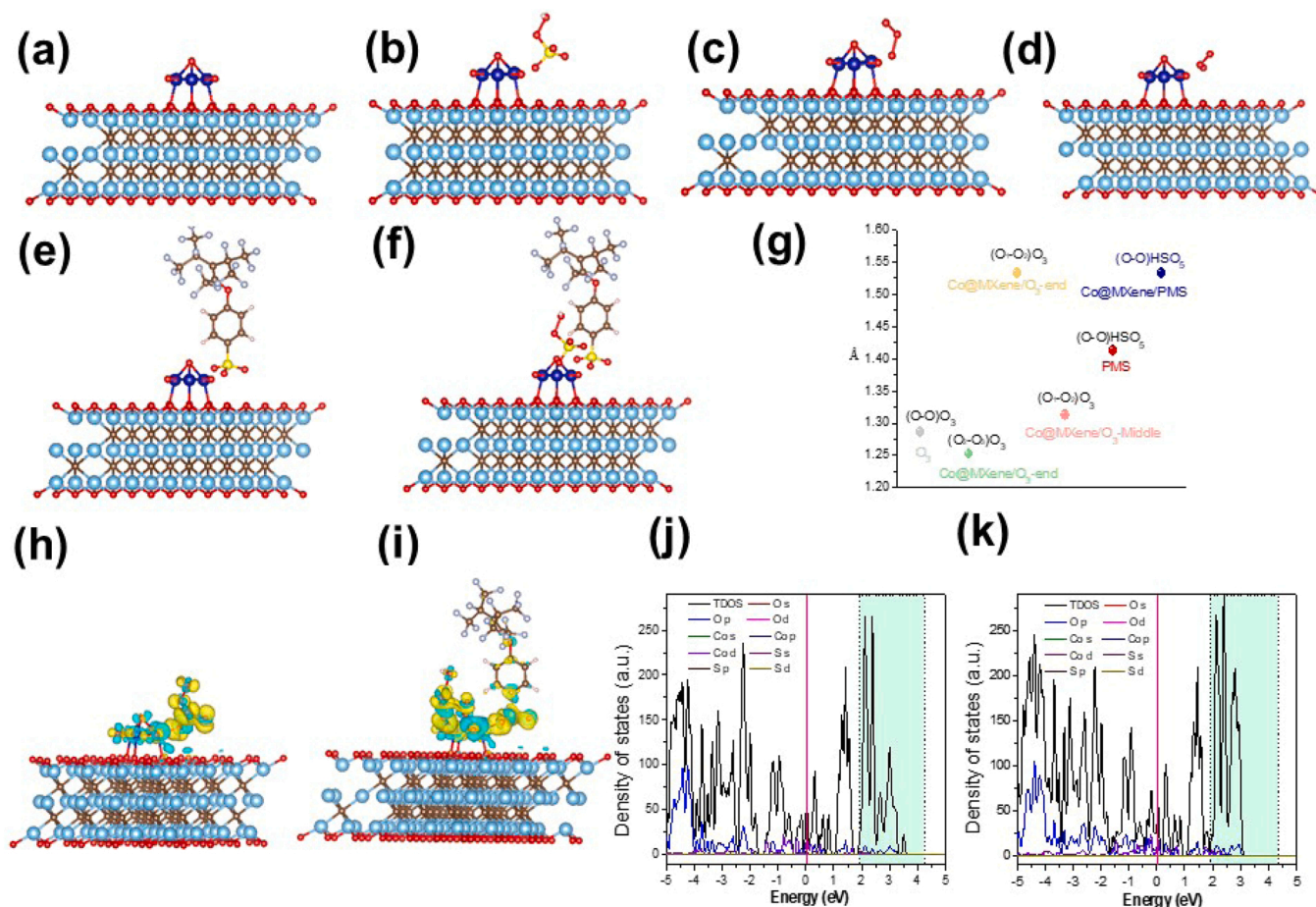


Fig. 7. (a–f) Optimized configurations (a* axis view) of Co@o-MXene, Co@o-MXene/PMS, Co@o-MXene/O₃ (edge O), Co@o-MXene/O₃ (middle O), Co@o-MXene/OBS and Co@o-MXene/OBS/PMS, respectively. (g) Bond length of O–O in different structure. Schematic of the (h) Co@o-MXene/PMS and (i) Co@o-MXene/OBS/PMS differential charge density (yellow and cyan represent charge accumulation and depletion, respectively). (j) and (k) The computed DOS of Co@o-MXene/PMS and Co@o-MXene/OBS/PMS. The red, brown, yellow, navy-blue, sky-blue, light gray and salmon spheres are O, C, S, Co, Ti, F and H atoms, respectively.

were the vulnerable sites by ROSs. The role of pollutant during reaction could not be ignored and the Co \cdots SO₃ cation- π interaction was proposed. The TDOS results showed the enhanced π electrons from OBS were transferred to the Co²⁺ sites linked by the benzenesulfonic acid functional group after PMS complexation, which resulted in the effective O₃ and PMS utilization. The differential charge densities and HOEB-LUEB analysis exhibited the redistribution and efficient transfer of electrons would improve the catalytic oxidation process for via the unique Co \cdots SO₃ cation- π bridge.

CRediT authorship contribution statement

Shangyi Li: Methodology, Investigation, Writing – original draft, Data validation. **Mengbin Gu:** Investigation, Data validation. **Jun Huang:** Supervision, Funding acquisition, Writing – review & editing. **Yujue Wang & Gang Yu:** Discussion, Supervision.

Declaration of Competing Interest

The authors declare that they have no known competing financial interests or personal relationships that could have appeared to influence the work reported in this paper.

Acknowledgements

This work was supported by the National Natural Science Foundation of China (No. 22076092), the project of China Postdoctoral Science

Foundation (No. 2020TQ0165 and 2021M691768).

Appendix A. Supporting information

Supplementary data associated with this article can be found in the online version at [doi:10.1016/j.apcatb.2022.121364](https://doi.org/10.1016/j.apcatb.2022.121364).

References

- [1] L. Fu, K. Liao, J. Ge, Y. He, W. Guo, S. Zhang, Synergistic effect of sodium p-perfluorononyloxybenzenesulfonate and alkanolamide compounding system used as cleanup additive in hydraulic fracturing, *Energy Fuels* 34 (2020) 7029–7037.
- [2] J.M. Conder, R.A. Hoke, W. De Wolf, M.H. Russell, R.C. Buck, Are PFCAs bioaccumulative? A critical review and comparison with regulatory lipophilic compounds, *Environ. Sci. Technol.* 42 (2008) 995–1003.
- [3] Y. Bao, Y. Qu, J. Huang, G. Cagnetta, G. Yu, R. Weber, First assessment on degradability of sodium p-perfluorooctanoxybenzene sulfonate (OBS), a high volume alternative to perfluorooctane sulfonate in fire-fighting foams and oil production agents in China, *RSC Adv.* 7 (2017) 46948–46957.
- [4] L. Xu, Y. Shi, C. Li, X. Song, Z. Qin, D. Cao, Y. Cai, Discovery of a novel polyfluoroalkyl benzenesulfonic acid around oilfields in northern China, *Environ. Sci. Technol.* 51 (2017) 14173–14181.
- [5] M. Zhao, X. Ni, S. Zhang, W. Cao, Y. Guan, C. Liang, X. Wang, H. Zhang, Improving the performance of fluoroprotein foam in extinguishing gasoline pool fires with addition of bromofluoropropene, *Fire Mater.* 40 (2016) 261–272.
- [6] W. Tu, R. Martinez, L. Navarro-Martin, D.J. Kostyniuk, C. Hum, J. Huang, M. Deng, Y. Jin, H.M. Chan, J.A. Mennigen, Bioconcentration and metabolic effects of emerging PFOS alternatives in developing zebrafish, *Environ. Sci. Technol.* 53 (2019) 13427–13439.

- [7] Y. Ke, J. Chen, X. Hu, T. Tong, J. Huang, S. Xie, Emerging perfluoroalkyl substance impacts soil microbial community and ammonia oxidation, *Environ. Pollut.* 257 (2020), 113615.
- [8] W. Qiao, Z. Xie, Y. Zhang, X. Liu, S. Xie, J. Huang, L. Yu, Perfluoroalkyl substances (PFASs) influence the structure and function of soil bacterial community: greenhouse experiment, *Sci. Total Environ.* 642 (2018) 1118–1126.
- [9] C. Wang, Y. Zhang, M. Deng, X. Wang, W. Tu, Z. Fu, Y. Jin, Bioaccumulation in the gut and liver causes gut barrier dysfunction and hepatic metabolism disorder in mice after exposure to low doses of OBS, *Environ. Int.* 129 (2019) 279–290.
- [10] J. Zhang, H. Pang, S. Gray, S. Ma, Z. Xie, L. Gao, PFAS removal from wastewater by in-situ formed ferric nanoparticles: Solid phase loading and removal efficiency, *J. Environ. Chem. Eng.* 9 (2021), 105452.
- [11] R. Thomas, K. Jenkins, B. Landale, G. Trigger, T.M. Holsen, S. Dore, D. Pope Jr., J. Wasielewski, Evaluation of PFAS treatment technology: alkaline ozonation, *Remediat. - J. Environ. Cleanup Costs Technol. Tech.* 30 (2020) 27–37.
- [12] X. Dai, Z. Xie, B. Dorian, S. Gray, J. Zhang, Comparative study of PFAS treatment by UV, UV/ozonation, and fractionations with air and ozonated air, *Environ. Sci. Water Res. Technol.* 5 (2019) 1897–1907.
- [13] V. Franke, M.D. Schafers, J.J. Lindberg, L. Ahrens, Removal of per- and polyfluoroalkyl substances (PFASs) from tap water using heterogeneously catalyzed ozonation, *Environ. Sci. Water Res. Technol.* 5 (2019) 1887–1896.
- [14] N.M. Robey, B.F. da Silva, M.D. Annable, T.G. Townsend, J.A. Bowden, Concentrating per- and polyfluoroalkyl substances (PFAS) in municipal solid waste landfill leachate using foam separation, *Environ. Sci. Technol.* 54 (2020) 12550–12559.
- [15] P. Meng, S. Deng, X. Lu, Z. Du, B. Wang, J. Huang, Y. Wang, G. Yu, B. Xing, Role of air bubbles overlooked in the adsorption of perfluorooctanesulfonate on hydrophobic carbonaceous adsorbents, *Environ. Sci. Technol.* 48 (2014) 13785–13792.
- [16] C. VonSonntag, U. VonGunten, *Chemistry of Ozone in Water and Wastewater Treatment: From Basic Principles to Applications*, IWA Publishing, 2012.
- [17] W.R. Chen, X.K. Li, Z.Q. Pan, S.S. Ma, L.S. Li, Effective mineralization of Diclofenac by catalytic ozonation using Fe-MCM-41 catalyst, *Chem. Eng. J.* 304 (2016) 594–601.
- [18] H.H. Yan, W.R. Chen, G.Z. Liao, X.K. Li, S.S. Ma, L.S. Li, Activity assessment of direct synthesized Fe-SBA-15 for catalytic ozonation of oxalic acid, *Sep. Purif. Technol.* 159 (2016) 1–6.
- [19] S. Li, J. Huang, Y. Wang, G. Yu, Role of in-situ electro-generated H₂O₂—bridge in tetracycline degradation governed by mechanochemical Si-O anchoring Cu₂+ as electron shuttle during E-peroxone process, *Appl. Catal. B Environ.* 304 (2021), 120930.
- [20] S.Y. Li, J. Huang, X.K. Li, L.S. Li, The relation of interface electron transfer and PMS activation by the H-bonding interaction between composite metal and MCM-48 during sulfamethazine ozonation, *Chem. Eng. J.* 398 (2020), 125529.
- [21] S. Li, X. Fan, M. Gu, G. Cagnetta, J. Huang, G. Yu, Confined-space strategy for anchoring catalytic nanoparticles on Si-OH by ball milling for enhanced O₃/PMS oxidation of ciprofloxacin, *Chem. Eng. J.* 429 (2022), 132318.
- [22] Y.X. Mao, H.Y. Dong, S.G. Liu, L.P. Zhang, Z.M. Qiang, Accelerated oxidation of iopamidol by ozone/peroxymonosulfate (O-3/PMS) process: kinetics, mechanism, and simultaneous reduction of iodinated disinfection by-product formation potential, *Water Res.* 173 (2020), 115615.
- [23] M. Naguib, M. Kurtoglu, V. Presser, J. Lu, J. Niu, M. Heon, L. Hultman, Y. Gogotsi, M.W. Barsoum, Two-dimensional nanocrystals produced by exfoliation of Ti₃AlC₂, *Adv. Mater.* 23 (2011) 4248–4253.
- [24] L. Ding, Y. Wei, Y. Wang, H. Chen, J. Caro, H. Wang, A. Two-Dimensional, Lamellar membrane: MXene nanosheet stacks, *Angew. Chem. -Int. Ed.* 56 (2017) 1825–1829.
- [25] L. Hu, R. Xiao, X. Wang, X. Wang, C. Wang, J. Wen, W. Gu, C. Zhu, MXene-induced electronic optimization of metal-organic framework-derived CoFe LDH nanosheet arrays for efficient oxygen evolution, *Appl. Catal. B Environ.* 298 (2021), 120599.
- [26] Y. Liu, R. Luo, Y. Li, J. Qi, C. Wang, J. Li, X. Sun, L. Wang, Sandwich-like Co₃O₄/MXene composite with enhanced catalytic performance for bisphenol A degradation, *Chem. Eng. J.* 347 (2018) 731–740.
- [27] D. Xu, Y. Ma, J. Wang, W. Chen, Y. Tang, X. Li, L. Li, Interfacial engineering of 2D/2D MXene heterostructures: face-to-face contact for augmented photodegradation of amoxicillin, *Chem. Eng. J.* 426 (2021), 131246.
- [28] Y. Ma, D. Xu, W. Chen, Y. Tang, X. Wang, L. Li, J. Wang, Oxygen-vacancy-embedded 2D/2D NiFe-LDH/MXene Schottky heterojunction for boosted photodegradation of norfloxacin, *Appl. Surf. Sci.* 572 (2022), 151432.
- [29] Y. Xie, M. Naguib, V.N. Mochalin, M.W. Barsoum, Y. Gogotsi, X. Yu, K.-W. Nam, X.-Q. Yang, A.I. Kolesnikov, P.R.C. Kent, Role of surface structure on Li-ion energy storage capacity of two-dimensional transition-metal carbides, *J. Am. Chem. Soc.* 136 (2014) 6385–6394.
- [30] J. Luo, C. Fang, C. Jin, H. Yuan, O. Sheng, R. Fang, W. Zhang, H. Huang, Y. Gan, Y. Xia, C. Liang, J. Zhang, W. Li, X. Tao, Tunable pseudocapacitance storage of MXene by cation pillaring for high performance sodium-ion capacitors, *J. Mater. Chem. A* 6 (2018) 7794–7806.
- [31] X. Song, H. Wang, S. Jin, M. Lv, Y. Zhang, X. Kong, H. Xu, T. Ma, X. Luo, H. Tan, D. Hu, C. Deng, X. Chang, J. Xu, Oligolayered Ti₃C₂T_x MXene towards high performance lithium/sodium storage, *Nano Res.* 13 (2020) 1659–1667.
- [32] N. Jaafarzadeh, F. Ghanbari, M. Ahmadi, Efficient degradation of 2,4-dichlorophenoxyacetic acid by peroxymonosulfate/magnetic copper ferrite nanoparticles/ ozone: a novel combination of advanced oxidation processes, *Chem. Eng. J.* 320 (2017) 436–447.
- [33] A. Lagutschenkov, R.K. Sinha, P. Maitre, O. Dopfer, Structure and infrared spectrum of the Ag⁺-phenol ionic complex, *J. Phys. Chem. A* 114 (2010) 11053–11059.
- [34] Y. Wang, L. Lyu, D. Wang, H.-Q. Yu, T. Li, Y. Gao, F. Li, J.C. Crittenden, L. Zhang, C. Hu, Cation- π induced surface cleavage of organic pollutants with -OH formation from H₂O for water treatment, *Isience* 24 (2021), 102874.
- [35] L.M. Salonen, M. Ellermann, F. Diederich, Aromatic rings in chemical and biological recognition: energetics and structures, *Angew. Chem. -Int. Ed.* 50 (2011) 4808–4842.
- [36] H. Zhang, L. Lyu, Q. Fang, C. Hu, S. Zhan, T. Li, Cation- π structure inducing efficient peroxymonosulfate activation for pollutant degradation over atomically dispersed cobalt bonding graphene-like nanospheres, *Appl. Catal. B Environ.* 286 (2021), 119912.
- [37] S. Zhan, H. Zhang, X. Mi, Y. Zhao, C. Hu, L. Lyu, Efficient Fenton-like process for pollutant removal in electron-rich/poor reaction sites induced by surface oxygen vacancy over cobalt-zinc oxides, *Environ. Sci. Technol.* 54 (2020) 8333–8343.
- [38] L. Lyu, D. Yan, G. Yu, W. Cao, C. Hu, Efficient destruction of pollutants in water by a dual-reaction center Fenton-like process over carbon nitride compounds-complexed Cu(II)-CuAlO₂, *Environ. Sci. Technol.* 52 (2018) 4294–4304.
- [39] Q. Huang, J. Zhang, Z. He, P. Shi, X. Qin, W. Yao, Direct fabrication of lamellar self-supporting Co₃O₄/N/C peroxymonosulfate activation catalysts for effective aniline degradation, *Chem. Eng. J.* 313 (2017) 1088–1098.
- [40] Y. Sun, S. Gao, F. Lei, J. Liu, L. Liang, Y. Xie, Atomically-thin non-layered cobalt oxide porous sheets for highly efficient oxygen-evolving electrocatalysts, *Chem. Sci.* 5 (2014) 3976–3982.
- [41] S. Gao, X. Jiao, Z. Sun, W. Zhang, Y. Sun, C. Wang, Q. Hu, X. Zu, F. Yang, S. Yang, L. Liang, J. Wu, Y. Xie, Ultrathin Co₃O₄ layers realizing optimized CO₂ electroreduction to formate, *Angew. Chem. -Int. Ed.* 55 (2016) 698–702.
- [42] W.-D. Oh, Z. Dong, Z.-T. Hu, T.-T. Lim, A novel quasi-cubic CuFe₂O₄-Fe₂O₃ catalyst prepared at low temperature for enhanced oxidation of bisphenol A via peroxymonosulfate activation, *J. Mater. Chem. A* 3 (2015) 22208–22217.
- [43] F. Ji, C. Li, X. Wei, J. Yu, Efficient performance of porous Fe₂O₃ in heterogeneous activation of peroxymonosulfate for decolorization of Rhodamine B, *Chem. Eng. J.* 231 (2013) 434–440.
- [44] Y. Lin, C. Ferronato, N. Deng, F. Wu, J.-M. Chovelon, Photocatalytic degradation of methylparaben by TiO₂: multivariable experimental design and mechanism, *Appl. Catal. B Environ.* 88 (2009) 32–41.
- [45] P. Neta, J. Grodkowski, A.B. Ross, Rate constants for reactions of aliphatic carbon-centered radicals in aqueous solution, *J. Phys. Chem. Ref. Data* 25 (1996) 709–1050.
- [46] C. Liang, Z.-S. Wang, N. Mohanty, Influences of carbonate and chloride ions on persulfate oxidation of trichloroethylene at 20 degrees C, *Sci. Total Environ.* 370 (2006) 271–277.
- [47] C.A.J. Appelo, M.J.J. Van der Weiden, C. Tournassat, L. Charlet, Surface complexation of ferrous iron and carbonate on ferrihydrite and the mobilization of arsenic, *Environ. Sci. Technol.* 36 (2002) 3096–3103.
- [48] H. Zhao, Y. Dong, G. Wang, P. Jiang, J. Zhang, L. Wu, K. Li, Novel magnetically separable nanomaterials for heterogeneous catalytic ozonation of phenol pollutant: NiFe₂O₄ and their performances, *Chem. Eng. J.* 219 (2013) 295–302.
- [49] E.D. Black, E. Hayon, Pulse radiolysis of phosphate anions H₂PO₄⁻, HPO₄²⁻, PO₄³⁻, and P₂O₇⁴⁻ in aqueous solutions, *J. Phys. Chem.* 74 (1970) 3199–3203.
- [50] D.O. Martire, M.C. Gonzalez, Aqueous phase kinetic studies involving intermediates of environmental interest: phosphate radicals and their reactions with substituted benzenes, *Prog. React. Kinet. Mech.* 26 (2001) 201–218.
- [51] P. Duan, X. Liu, B. Liu, M. Akram, Y. Li, J. Pan, Q. Yue, B. Gao, X. Xu, Effect of phosphate on peroxymonosulfate activation: accelerating generation of sulfate radical and underlying mechanism, *Appl. Catal. B Environ.* 298 (2021), 120532.
- [52] J.E. Grebel, J.J. Pignatello, W.A. Mitch, Effect of halide ions and carbonates on organic contaminant degradation by hydroxyl radical-based advanced oxidation processes in saline waters, *Environ. Sci. Technol.* 44 (2010) 6822–6828.
- [53] J. Wang, S. Wang, Effect of inorganic anions on the performance of advanced oxidation processes for degradation of organic contaminants, *Chem. Eng. J.* 411 (2021), 128392.
- [54] R. Tenorio, J.Y. Liu, X. Xiao, A. Maizel, C.P. Higgins, C.E. Schaefer, T. J. Strathmann, Destruction of Per- and polyfluoroalkyl substances (PFASs) in aqueous film-forming foam (AFFF) with uv-sulfite photoreductive treatment, *Environ. Sci. Technol.* 54 (2020) 6957–6967.
- [55] P. Neta, R.E. Huie, A.B. Ross, Rate constants for reactions of inorganic radicals in aqueous-solution, *J. Phys. Chem. Ref. Data* 17 (1988) 1027–1284.
- [56] R. Yin, Y. Chen, J. Hu, G. Lu, L. Zeng, W. Choi, M. Zhu, Complexes of Fe(III)-organic pollutants that directly activate Fenton-like processes under visible light, *Appl. Catal. B Environ.* 283 (2021), 119663.
- [57] S. Lan, B. Jing, C. Yu, D. Yan, Z. Li, Z. Ao, M. Zhu, Protrudent iron single-atom accelerated interfacial piezoelectric polarization for self-powered water motion triggered Fenton-like reaction, *Small* 18 (2022), 2105279.
- [58] J. Liang, Y. Jiao, M. Jaroniec, S.Z. Qiao, Sulfur and nitrogen dual-doped mesoporous graphene electrocatalyst for oxygen reduction with synergistically enhanced performance, *Angew. Chem. -Int. Ed.* 51 (2012) 11496–11500.